RSC Advances

ROYAL SOCIETY OF CHEMISTRY

PAPER

Check for updates

Cite this: *RSC Adv.*, 2020, **10**, 34403

MOF-derived manganese oxide/carbon nanocomposites with raised capacitance for stable asymmetric supercapacitor†

By Ruoyu Wang, Yating Hu, Zhenghui Pan * and John Wang *

Owing to immense application potentials in electrochemical energy storages, metal organic framework (MOF)-derived metal oxide/carbon nanocomposites have attracted extensive interest of research. Although thermolysis has been widely employed to convert MOFs into various active materials, a large set of *in situ* changes in chemical composition, phase(s) and morphology requires delicate control over heating parameters. Through an innovative two-stage process, Mn-MIL-100 is first transformed into MnO@C by annealing at 700 °C under N_2 flow, which is then transformed into Mn_3O_4@C at 200 °C in air, while retaining a high surface area. The appropriate retention of carbon content for Mn_3O_4@C can also be easily obtained with the control of heating time. In contrast, thermolysis of MnO@C at higher temperatures gives rise to manganese oxides with negligible carbon content and a greatly reduced surface area. The optimized Mn_3O_4@C-2 h, derived from MnO@C at 200 °C for 2 hours, showed the highest capacitance, far exceeding that of MnO@C and other derivatives. When combined with graphene oxide (GO) nanosheets to form a flexible Mn_3O_4@C/rGO paper electrode, it demonstrated a capacitance of 328.4 F cm^{-3}. The Mn_3O_4@C/rGO-based asymmetric supercapacitor thus assembled also shows favorable performance. The present work demonstrates the excellent controllability afforded by the innovative two-stage thermolysis in optimizing the electrochemical performance of MOF-derived active materials as electrode materials in supercapacitors.

Received 23rd June 2020
Accepted 2nd September 2020

DOI: 10.1039/d0ra05494a

rsc.li/rsc-advances

1. Introduction

Metal–Organic Frameworks (MOFs) are a class of crystalline materials formed through coordination bonds among metal ions and organic ligands.[1] They have gained substantial popularity in recent years as a group of novel materials, mainly due to their diverse structures, high levels of porosity and a high degree of tunability which expands their applications from gas absorption, separation, catalysis, drug delivery to energy storages.[1–5] Besides being directly utilized as functional materials, MOFs may also be precursors for the synthesis of various porous active structures, such as, nanoporous carbon, metal oxides, metal monoxides and metal oxides/monoxides/carbon nanocomposites.[6–11] Among various MOF-derivatives, the metal oxide/carbon nanocomposites are a family of potentially attractive supercapacitor electrode materials, due to the integration of carbon and active materials within a nanoporous structure.[12–14]

Transition metal oxides (TMOs), such as, Co_3O_4, NiO, and MnO_2, have long been regarded as prominent pseudocapacitance materials; however, they are also dragged in this regard by low electrical conductivities, poor stability and generally a small surface area for TMOs derived from normal hydrothermal processes.[15–22] Thanks to the highly tunable nature of MOFs, the MOF-derived metal oxide/carbon nanocomposites can be made to possess a very high surface area, which would increase the available redox-active sites and overall performance.[23] Moreover, the intrinsically poor electrical conductivity of metal oxides can be mitigated by integration with carbon content at the nanoscale.[23] Therefore, MOF-derived metal oxide/carbon nanocomposites are emerging as high-performance electrode materials for supercapacitors and other energy storage applications.[24–27]

Manganese oxides are an important family of TMO-based pseudocapacitance materials that exhibit several advantages, including, high theoretical capacitance, abundance, and environment friendliness. However, like other TMO materials, their performance is affected by poor electrical conductivity and low surface area, when derived from the conventional solution processing routes.[28–31] To improve the capacitance of manganese oxides, especially upon high loading mass, an apparent strategy is to develop MOF-derived manganese oxide/carbon nanocomposites, as mentioned above.[29] According to Das and *et al.*, it is feasible to transform Mn-MOFs into manganese oxide/carbon nanocomposites by calcination in an inert

Department of Materials Science and Engineering, National University of Singapore, Singapore 117574, Singapore. E-mail: msewangj@nus.edu.sg

† Electronic supplementary information (ESI) available. See DOI: 10.1039/d0ra05494a

This article is licensed under a Creative Commons Attribution-NonCommercial 3.0 Unported Licence.

(cc) BY-NC

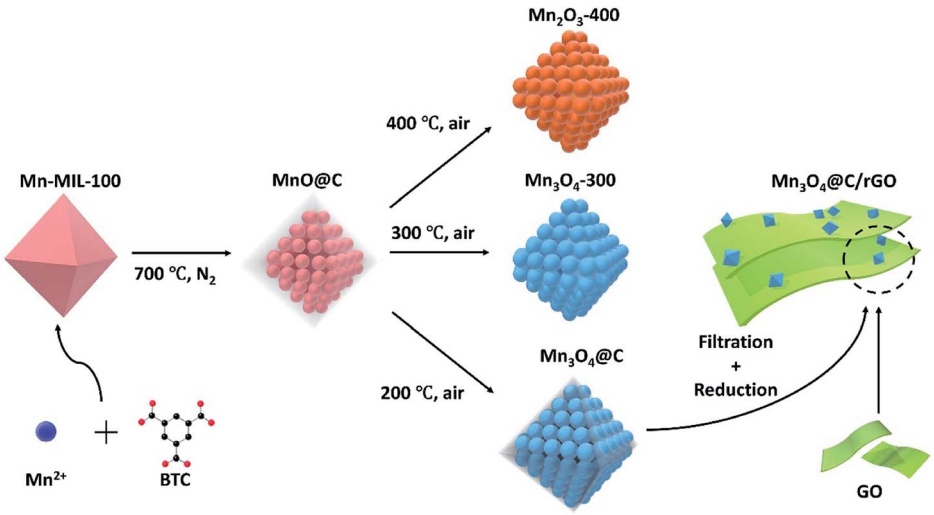

Scheme 1 Schematic illustration of the experimental procedure in this work.

atmosphere.[32] Nevertheless, MnO_x is one of the rather complicated oxides with variable valences, phases and structures. Therefore, to derive a manganese oxide/carbon nanocomposite with optimized performance from MOFs, several factors need to be controlled, such as, the chemical composition of manganese oxide, specific surface area, amount and scale of carbon content, and their combinations, all strongly affected by thermolysis conditions.[8,33,34] While MOF-derived manganese oxide/carbon nanocomposites are traditionally produced through a facile, one-step calcination in N_2, they can be further modified by post-annealing thermolysis, adding a new dimension to the controllability.[35] Thus, it would be of interest to study how these modifications can further vary the MOF-derived manganese oxide/carbon nanocomposite, and the impact such variations could have on the overall electrochemical performance.

Herein, MOF-derived MnO@C was subjected to thermolysis in air at various temperatures for different periods to investigate how the chemical, phase and morphological properties of the MnO@C would change. Interestingly, proper thermolysis in air at a moderate temperature of 200 °C would transform MnO@C into Mn_3O_4@C, which would retain the high surface area and part of the carbon content from the original MnO@C. On the contrary, upon thermolysis in air at 300 and 400 °C, the MnO@C would transform into Mn_3O_4-300 and Mn_2O_3-400, respectively, with negligible carbon content and a much-reduced surface area as compared to that of the MnO@C. Electrochemical measurements revealed that the Mn_3O_4@C sample being thermolyzed for 2 h (Mn_3O_4@C-2 h) shows the highest capacitance, far exceeding that of both Mn_3O_4-300 and Mn_2O_3-400, as well as the original MnO@C, indicating the importance of controlling the thermolysis conditions. To further demonstrate the potential of the MOF-derived manganese oxide/carbon nanocomposite, the Mn_3O_4@C-2 h with optimum performance is combined with aqueous graphene oxide (GO) nanosheets to form a flexible Mn_3O_4@C paper by vacuum filtration, which is then electrochemically reduced (denoted as Mn_3O_4@C/rGO) to improve the electrical conductivity. The Mn_3O_4@C/rGO thus made exhibited volumetric capacitance as high as 328.4 F cm^{-3} at 0.5 A cm^{-3}. An asymmetric aqueous supercapacitor was then fabricated with the Mn_3O_4@C/rGO as the positive and the carbon nanotube (CNT)/rGO as the negative electrode, respectively. The asymmetric supercapacitor duly demonstrates the viability of the MOF-derived manganese oxide/carbon nanocomposites obtained through the two-stage thermolysis as a class of promising supercapacitor materials. The experimental procedures in this work are briefly summarized in Scheme 1.

2. Results and discussion

2.1 Materials synthesis and characterization

To synthesize a MOF-derived manganese oxide/carbon nanocomposite, it is essential to select an appropriate MOF as the precursor, since the products of MOF pyrolysis, to some extent, inherit the morphology of the parent MOF. In this work, Mn-MIL-100 MOF was selected for its large pores (25 Å and 29 Å, respectively) and a high surface area of 1540 m^2 g^{-1}, which is one of the best among the Mn-MOFs.[36] The Mn-MIL-100 (Fig. S1†) was synthesized by a modified solvothermal method (the details can be found in the Experimental section).[36] The Mn-MIL-100 MOF was then calcined at 700 °C for 2 hours in a tube furnace under nitrogen airflow to obtain the MnO@C.[37–39] After cooling to room temperature, the black powdered product was recovered and characterized. As shown in Fig. 1a, the powder X-ray diffraction (XRD) patterns indicate the formation of MnO nanoparticles within the product. The widened diffraction peaks also suggest a small degree of crystallinity according to the Scherrer equation.[40] From the scanning electron microscopy (SEM) results, the polyhedron shape of the parent MOF was well preserved (Fig. S2† and 1b), and the corresponding EDS mapping confirmed the presence of Mn, O and C elements (Fig. 1b). It should be noted that since there is no peak corresponding to the crystalline carbon in the XRD pattern, the product should be a nanocomposite of MnO and

 This journal is © The Royal Society of Chemistry 2020

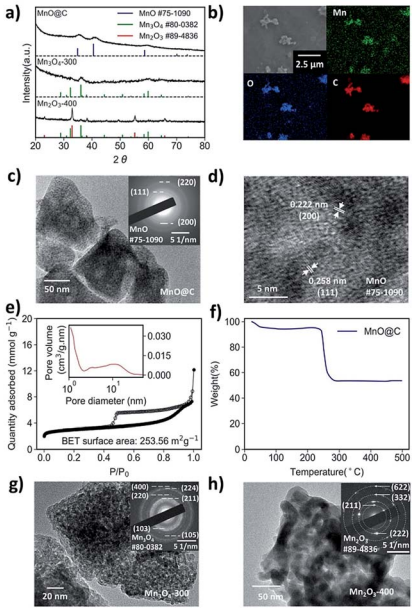

Fig. 1 Comparison of the (a) EIS, and (b) CV results between Mn_3O_4@C/GO and Mn_3O_4@C/rGO. (c) Cross-section SEM of Mn_3O_4@C/rGO. (d) TEM and SAED of Mn_3O_4@C/rGO. (e) CV curves, (f) GCD curves, (g) volumetric capacitance, and (h) cyclic test results of Mn_3O_4@C/rGO.

amorphous carbon.[41] The morphology was further investigated by transmission electron microscopy (TEM), where MnO nanoparticles with an average size of around 10 nm were embedded within a carbon matrix, suggesting a MnO@C core/shell nanostructure (Fig. 1c and d), with the lattice fringes of the MnO particles being visible (Fig. 1d). The N_2 adsorption/desorption isotherm of MnO@C corresponds to a type IV isotherm with a type H4 hysteresis loop, which is often found on micro-mesoporous carbon (Fig. 1e).[42] The DFT pore distribution of the MnO@C suggests the presence of both micro (1–2 nm) and mesopores (2–10 nm) (Fig. 1e inset), and the BET surface area for MnO@C was calculated to be 253.56 m^2 g^{-1}. TGA was also done to study the thermal stability and decomposition temperature of MnO@C (Fig. 1f). The sharp weight loss at around 250 °C can well be attributed to the carbon loss, from which a carbon content of more than 45 wt% was concluded. The product of TGA testing was found to be Mn_3O_4 by XRD (Fig. S3†). Therefore, a MnO@C nanoporous composite with a relatively high surface area of 253.56 m^2 g^{-1} and abundant carbon content of more than 45 wt% was successfully synthesized.[9,39]

To modify the key parameters, *e.g.*, chemical composition, phase and morphology, further thermolysis in air was carried out on the MOF-derived MnO@C. Based on the TGA study for MnO@C, we first investigated the thermolysis products above 250 °C, where a sudden carbon loss occurred. The heating of MnO@C at 300 °C in air for 2 hours transformed the MnO phase into Mn_3O_4 (Fig. 1a). The EDS mapping of the sample (denoted as Mn_3O_4-300) showed no bright contrast for carbon, indicating negligible carbon content (Fig. S4a†). The TEM image of sample Mn_3O_4-300 further indicated the missing carbon matrix as observed in sample MnO@C (Fig. 1g). The DFT pore distribution calculated from the N_2 isotherm (Fig. S5a†) revealed that the large micropores and the small mesopores of the original MnO@C, which contributed to the bulk of the surface area, were significantly reduced and enlarged, respectively, with a much smaller surface area of 91.26 m^2 g^{-1}. When a higher thermal treatment temperature of 400 °C was used, Mn_2O_3 particles formed after 2 hours, with some peaks belonging to Mn_3O_4 still being visible from XRD patterns (Fig. 1a). Since most manganese oxides had been readily transformed into Mn_2O_3, indicated by the relative peak intensity, the 400 °C sample was named Mn_2O_3-400. TEM studies of sample Mn_2O_3-400 showed particles of much larger grain size than those of sample Mn_3O_4-300 (Fig. 1h). As is the case for Mn_3O_4-300, negligible carbon remained in the Mn_2O_3-400 sample (Fig. S4b†), and the BET surface area was further reduced to 62.53 m^2 g^{-1} with larger but fewer pores (Fig. S5b†).

Compared to the original MnO@C, samples treated at both 300 °C and 400 °C have only negligible carbon content, and a much-decreased surface area, which would not be favorable for supercapacitor application. Therefore, we looked at more moderate heating parameters. Referring to the TGA results of the MnO@C (Fig. 1f), the sharp mass loss in association with carbon might be avoided at below 250 °C. Thus, thermolysis was carried out at 200 °C. At this temperature, the carbon loss proceeds at such a low rate that by variation of the heating period, the carbon content can be effectively controlled (Fig. 2a). Therefore, MnO@C samples were heated for 1.0 hour, 2.0 hours, and 5.0 hours, respectively. Upon heating for 1.0 hour, the MnO particles transformed into Hausmannite and became Mn_3O_4, as indicated by the XRD phase analysis shown in Fig. 2b (thus, the samples were denoted as Mn_3O_4@C-1 h, Mn_3O_4@C-2 h and Mn_3O_4@C-5 h, respectively). This transition from the rock salt MnO to spinel Mn_3O_4 Hausmannite at such a low temperature could well be related to the small size of the MnO particles.[43] The TEM studies (Fig. 2d–f) show that with increased heating time, the sample profile became rougher and the dark shades within the sample also became sharper. These changes suggest a slowing-down process of carbon depletion, which is also reflected in the XPS results (Fig. 2c), where the intensity of the peak corresponding to the C 1s electrons decreases with heating time. To verify how much carbon is still left, Mn_3O_4@C-5 h was subjected to another TGA study (Fig. S7†), where the characteristic slope at 200 °C suggests that around 15 wt% of carbon remained. The presence of significant carbon was further confirmed by the EDS mapping of Mn_3O_4@C-5 h (Fig. S6†), where the carbon element is visible. By analyzing N_2 isotherms (Fig. 1a, 2g–i), it was observed that the BET surface area of MnO@C increased to 336.07 m^2 g^{-1} when it became Mn_3O_4@C-1 h, before finally dropping to 236.46 m^2 g^{-1} after 5 hours of heating with some loss in porosity. All Mn_3O_4@C samples exhibited a BET surface area comparable to that of the original MnO@C, thanks to the moderate thermolysis temperature of 200 °C. Fig. S9† summarizes the thermolysis processes involved in this work and their respective products. It is worth noting that the MOF-derived Mn_3O_4@C exhibited a surface area

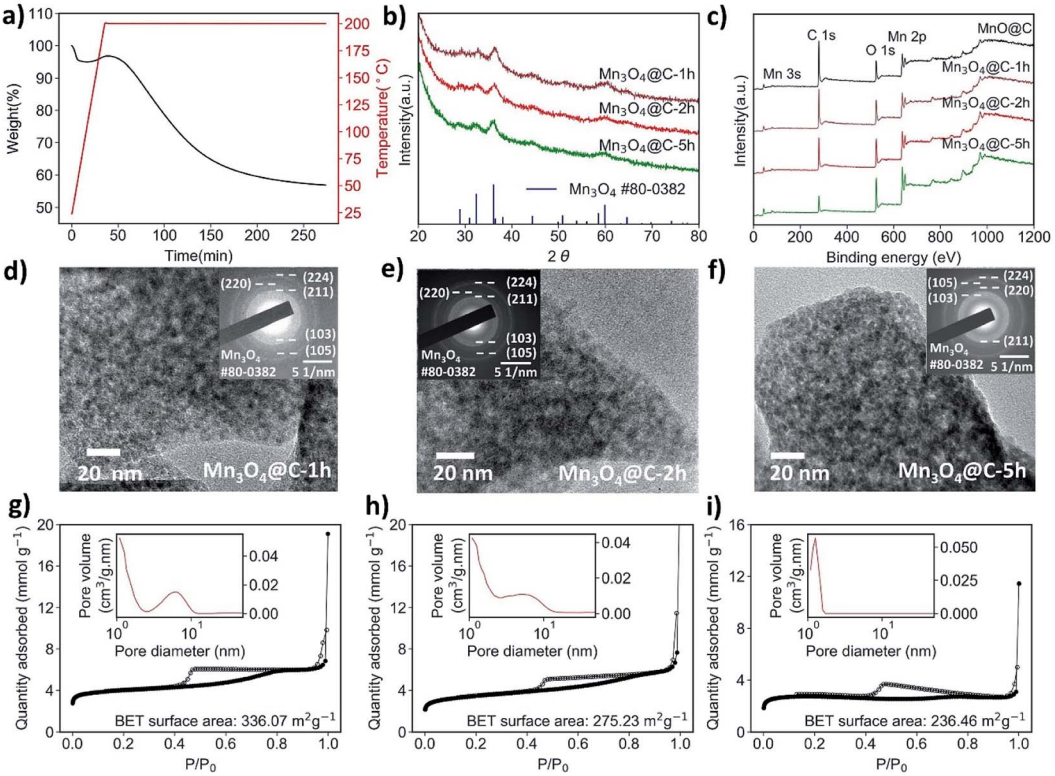

Fig. 2 (a) Heating profile (red line), and TGA analysis result (navy blue line) of the MnO@C held at 200 °C in air. (b) XRD traces of Mn_3O_4@C-1 h, Mn_3O_4@C-2 h and Mn_3O_4@C-5 h. (c) XRD results of various samples. TEM images of (d) Mn_3O_4@C-1 h, (e) Mn_3O_4@C-2 h and (f) Mn_3O_4@C-5 h. N_2 isotherms and DFT pore distributions of (g) Mn_3O_4@C-1 h, (h) Mn_3O_4@C-2 h and (i) Mn_3O_4@C-5 h.

comparable to those of some amorphous manganese oxides materials, which have attracted considerable attention due to the high surface area and excellent chemical stability.[41]

2.2 Electrochemical behavior of MOF-derived MnO_x@C

The chemical composition, phase and morphology of the metal oxide/carbon nanocomposites have a significant impact on the electrochemical performance. To study the effects of these factors and aim for the optimum sample with the highest capacitance, MnO@C and its various derivatives were subjected to electrochemical tests in a three-electrode system with 0.5 M Na_2SO_4 aqueous solution as the electrolyte. Contrary to the alkaline electrolyte (*e.g.*, KOH), in neutral electrolyte such as Na_2SO_4, in spite of the generally lower capacitance, Mn_3O_4 showed near-rectangular CV patterns and has demonstrated better cyclic stability, which are favorable for supercapacitor applications.[44,45] This difference can well originate from the different mechanisms for the pseudocapacitance of Mn_3O_4 when used in different electrolytes. Moreover, a neutral electrolyte is also safer and more facile to process. The capacitances of various samples are shown in Fig. 3. Surprisingly, the original MnO@C showed the worst gravimetric capacitance (only 2.1 F g^{-1}), despite a large surface area and a high carbon content. This lack of performance could be a result of the intrinsic capacitance of MnO and the excessive carbon preventing MnO from accessing the cations (Na^+) of the electrolyte.[46] The Mn_3O_4-300 and Mn_2O_3-400 were compared as shown in Fig. S10.† Although both exhibited much higher capacitance than that of the MnO@C, the latter was even better with a capacitance of 78.9 F g^{-1} at 0.2 A g^{-1}. Considering that negligible carbon content remained in both samples and that the Mn_2O_3-400 had the lower surface area, the results suggest the intrinsically better pseudocapacitance of Mn_2O_3, when compared to Mn_3O_4 in Na_2SO_4 aqueous electrolyte.

The Mn_3O_4@C samples thermolyzed at 200 °C were tested as shown in Fig. S11.† Though the Mn_3O_4@C-1 h demonstrated

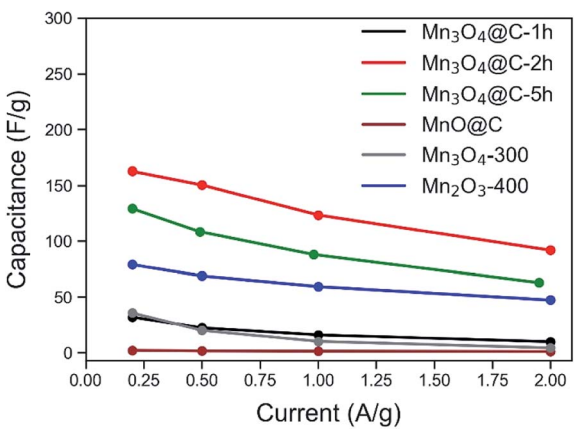

Fig. 3 Comparison of the gravimetric capacitances of various samples.

 This journal is © The Royal Society of Chemistry 2020

Table 1 A summary of various samples studied in this work

Sample	Chemical composition	BET surface area ($m^2\ g^{-1}$)	Est. carbon (wt%)	Capacitance ($F\ g^{-1}$)
MnO@C	MnO	253.56	45	2.1
Mn_3O_4-300	Mn_3O_4	91.26	Negligible	35.6
Mn_2O_3-400	Mn_2O_3/Mn_3O_4	62.53	Negligible	78.9
Mn_3O_4@C-1 h	Mn_3O_4	336.07	35	31.8
Mn_3O_4@C-2 h	Mn_3O_4	275.23	25	162.6
Mn_3O_4@C-5 h	Mn_3O_4	236.46	15	129.1

a huge improvement over the MnO@C (31.8 F g^{-1} at 0.2 A g^{-1}), it struggled to outperform the Mn_3O_4-300 with a much lower surface area. This may again indicate the negative effect of excessive carbon content. With the extension of heating time by another hour, the Mn_3O_4@C-2 h was much improved and showed the best capacitance values (162.6 F g^{-1} at 0.2 A g^{-1}) of all the samples. When the thermolysis at 200 °C in air was further extended to 5.0 hours, the capacitance decreased slightly to 129.1 F g^{-1} at 0.2 A g^{-1}.

The various Mn_3O_4@C nanocomposites demonstrated near-rectangular CV patterns (Fig. S11†) in accordance with the previously reported Mn_3O_4 pseudocapacitive materials in neutral electrolyte. The contribution of the double-layer capacitance relative to the overall capacitance of the best performing Mn_3O_4@C-2 h was estimated by Trassatti's method to be in the region of ~10% (Fig. S12†); the rest were diffusion-controlled. Although the mechanism for the pseudocapacitance of spinel Mn_3O_4 in a neutral electrolyte (*e.g.*, KCl, Na_2SO_4) has yet to be fully established, previous studies have suggested the reversible Mn(II)/Mn(III) redox reaction and intercalation/deintercalation of cation ions, which can be described as follows:[47,48]

$$MnO_x(OM)_y + zM^+ + ze^- = MnO_{x-z}(OM)_{y+z}$$

where M^+ represents the cations.[49]

Therefore, the improved capacitance of Mn_3O_4@C-2 h can be attributed to the better exposure of Mn_3O_4 to the electrolyte, whose pseudocapacitance makes up the majority of the capacitive performance. The slight decrease in the capacitance of Mn_3O_4@C-5 h was attributed to a lower surface area and degraded electrical conductivity, due to further changes in the carbon content. Table 1 lists the chemical state, phases, BET surface area and carbon content of various samples along with their respective capacitances at 0.2 A g^{-1}.

Based on the above discussions, the importance of appropriate carbon content and a high surface area is evident from the better performance of Mn_3O_4@C-2 h; it not only outperforms the Mn_3O_4-300, but it is also significantly better than Mn_2O_3-400. However, excessive carbon content is not desirable since it may hinder the interactions between manganese oxide and the electrolyte, as indicated by the lower capacitance of Mn_3O_4@C-1 h as compared to that of Mn_3O_4@C-2 h and the extremely low capacitance of MnO@C. It is worth noting that such a delicate control over the specific surface area and the carbon content is enabled by the two-stage thermolysis of Mn-MOF.

2.3 Electrochemical performance of Mn_3O_4@C/rGO

For a powdered material, *e.g.*, the Mn_3O_4@C in this work, it must be combined with a substrate playing the roles of both structural support and current collector. While the Ni foam-based electrode is sufficient for comparison purposes, it is far from ideal as even the best-performing Mn_3O_4@C-2 h electrode has a relatively low capacitance value, likely due to the severe agglomeration of Mn_3O_4@C particles. To solve this problem, we opted for a two-step strategy: firstly, combining the Mn_3O_4 powder with graphene oxide (GO) sheets by vacuum filtration to form a flexible nanohybrid-type paper; secondly, reducing the GO into conductive rGO (Fig. S13†). The as-prepared Mn_3O_4@C/

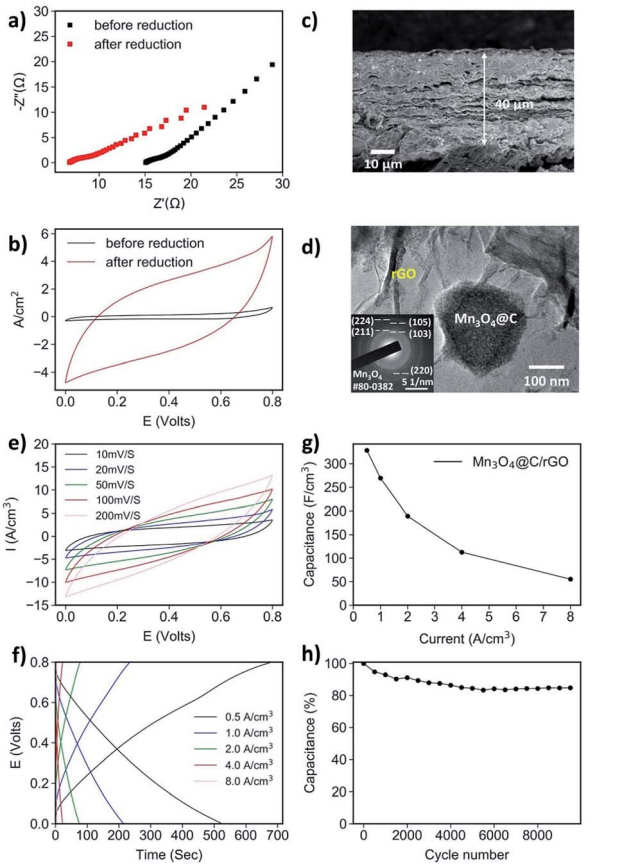

Fig. 4 Comparison of (a) EIS, and (b) CV results between Mn_3O_4@C/GO and Mn_3O_4@C/rGO. (c) Cross-section SEM of Mn_3O_4@C/rGO. (d) TEM and SAED of Mn_3O_4@C/rGO. (e) CV curves, (f) GCD curves, (g) volumetric capacitance, and (h) cyclic test results of Mn_3O_4@C/rGO.

GO paper exhibited a 3D-layered structure in which the Mn_3O_4@C polyhedrons are sandwiched by GO sheets (Fig. S14†). The layered structure facilitates better electrical conductivity as almost all Mn_3O_4@Cs are in contact with GO. Moreover, the paper demonstrated excellent mechanical flexibility (Fig. S15†). To preserve the flexible nature of the vacuum-filtered GO paper, a safe and facile method of electrochemical reduction was selected for GO reduction.[50,51]

The reduction of Mn_3O_4@C/GO paper was conducted in a three-electrode system with 0.5 M Na_2SO_4 aqueous electrolyte, and the process took 30 min at −1.5 V against the SCE reference electrode. To verify the effectiveness of the reduction, the EIS and CV of Mn_3O_4@C/GO before and after reduction were compared, as shown in Fig. 4a and b. The Z' value of the reduced sample was greatly decreased, suggesting a lower series resistance.[52] The reduced sample exhibited a greatly increased current when subjected to CV tests at 10 mV s^{-1} (Fig. 4d). Moreover, Raman spectroscopy of Mn_3O_4@C/GO and Mn_3O_4@C/rGO showed the D and G bands (at *ca.* 1350 and 1595 cm^{-1}, respectively), which are characteristic of graphite (Fig. S16a†). Upon reduction, the relative intensity of the D band increases due to the introduction of the sp^3 defects of carbon, indicating the partial reduction of GO.[53] The XPS results also suggest the successful reduction of GO (Fig. S16b†), as the peaks representing the C=O and the C–O bonds were greatly reduced relative to that of the C–C bond. Both the Mn_3O_4@C/rGO and Mn_3O_4@C/GO electrodes were subjected to TGA test in air (Fig. S17†). Due to the electrochemical reduction, which depletes oxygen from GO, there is less residue for the Mn_3O_4@C/rGO sample.[54] The mass loading of Mn_3O_4@C/rGO was estimated to be 0.85 g cm^{-3} (or 3.40 mg cm^{-2}, equivalently) from the TGA results, given an areal density of 7.60 mg cm^{-2}. More significantly, based on the SEM image (Fig. 4c), the layered structure was largely unaffected by the electrochemical reduction, with a thickness measured to be 40 μm. Due to the relatively weak diffraction of Mn_3O_4@C nanostructures dispersed within rGO sheets, XRD was not able to detect Mn_3O_4 crystals. Therefore, SAED was used to confirm that the Mn_3O_4 was intact after the electrochemical reduction (Fig. 4d-inset). From the TEM images, the Mn_3O_4@C sitting within the rGO sheet is visible (Fig. 4d, S18†). Hence, based on the collective results, the Mn_3O_4@C/rGO paper electrode, with uniform distribution, significantly improved electrical conductivity, and high mass loading, has been successfully prepared.

The electrochemical test on the Mn_3O_4@C/rGO was carried out in the same three-electrode system as in the case of electrochemical reduction. Before the test began, a comparative experiment was conducted between the Mn_3O_4@C/rGO and a pure rGO electrode of the same amount of rGO to verify that the capacitance directly generated from rGO only makes up a minor part and the Mn_3O_4@C is largely responsible for the capacitance (Fig. S19†). The volumetric capacitances of Mn_3O_4@C/rGO paper are illustrated in Fig. 4g. At a current density of 0.5 A cm^{-3}, the capacitance is as high as 328.4 F cm^{-3} (382.1 F g^{-1} for Mn_3O_4@C, estimated from mass loading), far exceeding that of the Mn_3O_4@C-2 h loaded on nickel foam. Even under a high current of 8.0 A cm^{-3}, a capacitance of 55.2 F cm^{-3} can still be retained. Such improvement is attributable to the fast electron transfer between rGO sheets and the Mn_3O_4@C particles enabled by the layered structure of Mn_3O_4@C.[54] Noted that an extremely high capacitance (exceeding 1000 F g^{-1}) can only be obtained at very low mass loading, while 100–200 F g^{-1} is usually achieved for MnO_x-based electrode when the mass loading is up to several milligrams per square centimeter.[23,26] Thus, the gravimetric capacitance established for Mn_3O_4@C/rGO is still a high value given its high mass loading. The electrode also exhibits a good endurance as capacitance retention of 85% is achieved after 10 000 of GCD cycles at 4 A cm^{-3} (Fig. 4h). Compared to previously reported Mn_3O_4/rGO hybrids of a similar design based on pure Mn_3O_4 nanoparticles, the Mn_3O_4@C/rGO exhibits a significant improvement in volumetric capacitance. For example, a Mn_3O_4/rGO paper (MGP) prepared achieved a capacitance of 109 F cm^{-3} at 0.2 A cm^{-3}.[43] In another work, an electrochemically reduced Mn_3O_4/rGO paper electrode, where the mass loading is estimated to be 0.71 g m^{-3}, exhibits a capacitance of 86.0 F cm^{-3} at 10 mV s^{-1}, still inferior to the Mn_3O_4@C/rGO paper in this work.[55] These results illustrate the advantage of the MOF-derived Mn_3O_4@C nanocomposite, with high surface area and improved electrical conductivity, as a supercapacitor electrode material when compared to pristine Mn_3O_4.

Upon the successful electrochemical reduction, the Mn_3O_4@C/rGO paper is formed into an aqueous asymmetric supercapacitor (AAS) with CNT/rGO as the negative electrode. The CNT/rGO is manufactured through a similar process to that of the Mn_3O_4@C/rGO, and the cross-section SEM is shown in Fig. S20.† The voltage window for the AAS is expected to be 0–1.8 V (Fig. 5a), as the CNT/rGO electrode has an effective working potential between −1.0 and 0.0 V (Fig. S21a†). The areal ratio between the two electrodes (positive/negative = 1/1.3) is

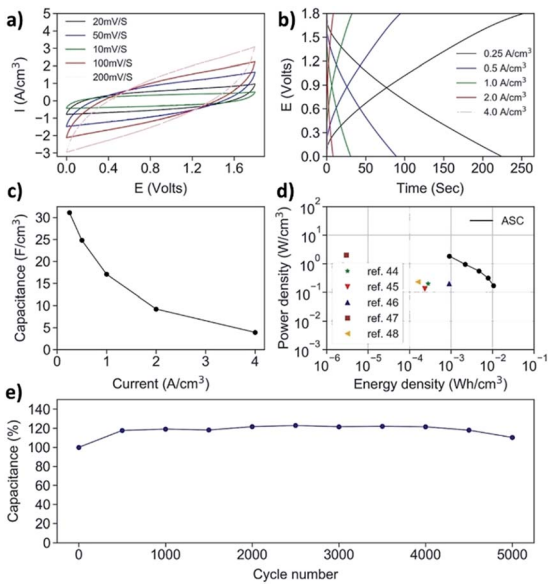

Fig. 5 (a) CV patterns, (b) GCD curves, (c) volumetric capacitance, (d) Ragone plot and (e) cyclic stability of the asymmetric aqueous supercapacitor.

This journal is © The Royal Society of Chemistry 2020

determined by their respective CV profiles at 10 mV s^{-1} (Fig. S21b†). The full device is tested in 0.5 M Na_2SO_4 electrolyte, and the volumes of both the negative and positive electrodes are taken into consideration of the volumetric capacitance, which is shown in Fig. 5c. The volumetric capacitance of the device reaches 31.13 F cm^{-3} at 0.25 A cm^{-3}. The assembled device could achieve an energy density of 10.6 mW h cm^{-3} with a power density of 0.17 W cm^{-3} (Fig. 5d). Even at a high-power output of 1.83 W cm^{-3}, an energy density of 0.9 mW h cm^{-3} can still be retained. A comparison with devices of reported works is made in Fig. 5d, where the results duly demonstrate the potential of Mn_3O_4@C/rGO as a supercapacitor electrode material. Furthermore, the stability test indicates that the AAS could withstand at least 5000 cycles of charge/discharge cycles at 4.0 A cm^{-3}, with an impressive capacitance retention of nearly 100% (Fig. 5e).[20,56–60]

3. Conclusion

Starting from Mn-MIL-100, several types of porous manganese oxides and manganese oxide/carbon nanocomposites were derived by a two-stage, successive thermolysis in nitrogen and air, where a series of changes in chemical composition, phase, morphology, level of porosity and carbon content can be controlled. Thermolysis in air at a moderate 200 °C transformed MOF-derived MnO@C into Mn_3O_4@C, while retaining a significant carbon content and high surface area of the original MnO@C, depending on heating time. On the contrary, MnO@C treated at 300 and 400 °C formed the Mn_3O_4 or Mn_2O_3 phase but with much-reduced porosity and negligible carbon content. When electrochemically tested in aqueous electrolyte, the Mn_3O_4@C-2 h sample showed the highest capacitance of all, due to an optimum balance of several factors, namely, the amount of carbon retained, high surface area and the desired phases of manganese oxides. A flexible nanocomposite-type Mn_3O_4@C/rGO paper incorporating Mn_3O_4@C-2 h was then prepared by vacuum filtration and electrochemical reduction, which enabled a volumetric capacitance of 328.4 F cm^{-3} at 0.5 A cm^{-3}. An asymmetric aqueous supercapacitor duly fabricated with the Mn_3O_4@C/rGO paper gave rise to an energy density of 10.6 mW h cm^{-3} at the power density of 0.17 W cm^{-3}.

4. Experimental section

4.1 Material synthesis

Mn-MIL-100 was synthesized by dissolving 500 mg of manganese(II) nitrate tetrahydrate ($Mn(NO_3)_2 \cdot 4H_2O$) and 900 mg of trimesic acid in to 20 ml of methanol, before transferring the solution into a 45 ml flask for solvothermal operation. The oven temperature was set to 125 °C for 2 hours before the sample was cooled to room temperature.

To prepare the nickel foam-based electrodes, of MnO@C powder or its derivatives were mixed with carbon black and polyvinylidene fluoride (PVDF) at a weight ratio of 8 : 1 : 1, followed by ultrasonication for 30 min. The well-dispersed mixture was then applied to clean nickel foam performing as the current collector. The as-prepared electrode was then dried in an oven at 60 °C overnight.

The Mn_3O_4@C/GO paper was prepared as follows: firstly, 30 mg of Mn_3O_4@C powder was mixed into 8 ml of 5 wt% GO aqueous dispersion with the addition of 4 ml deionized water (DI). The mixture was then extensively stirred by a magneton at a rate of 500 rpm for 24 h, followed by sonication for 1.0 h. After that, the well-dispersed Mn_3O_4@C/GO suspension was transferred into a Büchner funnel for vacuum filtration; a filter paper was placed in the bottom of the funnel before the filtration. After 6.0 h, the black Mn_3O_4@C/GO layer was formed on the filter paper. Finally, by immersing the paper into 95 wt% ethanol for 1.0 h, the Mn_3O_4@C/GO was separated from the filter paper due to the different extents of deformation upon contact with ethanol.

The CNT/rGO paper was prepared through a method similar to that of the Mn_3O_4@C/GO paper: a mixture of 30 mg of CNT fibers and 8 ml of 5 wt% GO aqueous dispersion was pressed into a paper by vacuum filtration before the same electrochemical reduction.

4.2 Materials characterizations

XRD patterns were collected on a BRUKER D8 X-ray diffractometer with a Cu Kα radiation source ($\lambda = 0.154$ nm). XPS was conducted with a Kratos Axis Ultra DLD photoelectron spectrometer. The morphology study was carried out with the aid of scanning electron microscopy (SUPRA 40 ZEISS, Germany) and transmission electron microscopy (JEOL 100CX 2010F, Japan). Raman scattering spectra were recorded on a LABRAM-HR Raman spectrometer with a 514.5 nm Ar^+ laser source. TA Instruments TGA Q500 was used for thermal analysis.

4.3 Electrochemical reduction and measurement

Electrochemical reduction of the Mn_3O_4@C/GO hybrid paper as the working electrode was performed in 0.5 M Na_2SO_4 aqueous solution at a potential of −1.5 V for 30 min. A Pt plate and a saturated calomel electrode were used as the counter electrode and the reference electrode, respectively. The electrochemical measurement of nickel foam-based electrode and the Mn_3O_4@C/rGO paper was carried out in the same setting. The voltage window was set at 0 to 0.8 V. For the electrical measurement of the asymmetric aqueous supercapacitor, Mn_3O_4@C/rGO paper and CNT/rGO paper were used as the cathode material and anode material, respectively. After matching their capacitance by adjusting their relative size, the two papers were assembled into a Swagelok cell for capacitance tests in 0.5 M Na_2SO_4 aqueous electrolyte. The voltage window for the full device was controlled at 0 to 1.8 V. CV and galvanostatic charge/discharge (GCD) measurements, and electrical impedance spectroscopy were conducted using the Solartron Systems 1470E and 1400A, respectively.

The working electrode was prepared by mixing MnO@C powder or its derivatives with carbon black and polyvinylidene fluoride (PVDF) as the conducting additive and binder, respectively, by a weight ratio of 8 : 1 : 1, followed by ultrasonication for 30 min. The well-dispersed mixture was then applied onto

clean nickel foam, performing as the current collector. The as-prepared electrode was then dried in an oven at 60 °C overnight. All the gravimetric performance parameters (*e.g.*, specific capacitance) in this work were calculated based on the mass of the active material; the weights of carbon black, binder and nickel foam were not included.

Conflicts of interest

There are no conflicts to declare.

Acknowledgements

We thank support of MOE, Singapore (Tier 1, R284-000-193-114) for funding of research, conducted at the National University of Singapore.

References

1 B. Li, H.-M. Wen, Y. Cui, W. Zhou, G. Qian and B. Chen, Emerging Multifunctional Metal–Organic Framework Materials, *Adv. Mater.*, 2016, **28**(40), 8819–8860.

2 J. Lee, O. K. Farha, J. Roberts, K. A. Scheidt, S. T. Nguyen and J. T. Hupp, Metal–Organic Framework Materials as Catalysts, *Chem. Soc. Rev.*, 2009, **38**(5), 1450–1459.

3 H. Wang, Q.-L. Zhu, R. Zou and Q. Xu, Metal–Organic Frameworks for Energy Applications, *Chem*, 2017, **2**(1), 52–80.

4 M. Wu and Y. Yang, Metal–Organic Framework (MOF)-Based Drug/Cargo Delivery and Cancer Therapy, *Adv. Mater.*, 2017, **29**(23), 1606134.

5 D. Sheberla, J. C. Bachman, J. S. Elias, C.-J. Sun, Y. Shao-Horn and M. Dincă, Conductive MOF Electrodes for Stable Supercapacitors with High Areal Capacitance, *Nat. Mater.*, 2017, **16**(2), 220–224.

6 W. Chaikittisilp, M. Hu, H. Wang, H.-S. Huang, T. Fujita, K. C.-W. Wu, L.-C. Chen, Y. Yamauchi and K. Ariga, Nanoporous Carbons through Direct Carbonization of a Zeolitic Imidazolate Framework for Supercapacitor Electrodes, *Chem. Commun.*, 2012, **48**(58), 7259.

7 W. Chaikittisilp, K. Ariga and Y. Yamauchi, A New Family of Carbon Materials: Synthesis of MOF-Derived Nanoporous Carbons and Their Promising Applications, *J. Mater. Chem. A*, 2013, **1**(1), 14–19.

8 R. R. Salunkhe, J. Tang, Y. Kamachi, T. Nakato, J. H. Kim and Y. Yamauchi, Asymmetric Supercapacitors Using 3D Nanoporous Carbon and Cobalt Oxide Electrodes Synthesized from a Single Metal–Organic Framework, *ACS Nano*, 2015, **9**(6), 6288–6296.

9 F. Zheng, G. Xia, Y. Yang and Q. Chen, MOF-Derived Ultrafine MnO Nanocrystals Embedded in a Porous Carbon Matrix as High-Performance Anodes for Lithium-Ion Batteries, *Nanoscale*, 2015, **7**(21), 9637–9645.

10 C. Guan, H. Wu, W. Ren, C. Yang, X. Liu, X. Ouyang, Z. Song, Y. Zhang, S. J. Pennycook, C. Cheng and J. Wang, Metal–Organic Framework-Derived Integrated Nanoarrays for Overall Water Splitting, *J. Mater. Chem. A*, 2018, **6**(19), 9009–9018.

11 X. Liu, C. Guan, Y. Hu, L. Zhang, A. M. Elshahawy and J. Wang, 2D Metal–Organic Frameworks Derived Nanocarbon Arrays for Substrate Enhancement in Flexible Supercapacitors, *Small*, 2018, **14**(43), 1702641.

12 W. Xia, A. Mahmood, R. Zou and Q. Xu, Metal–Organic Frameworks and Their Derived Nanostructures for Electrochemical Energy Storage and Conversion, *Energy Environ. Sci.*, 2015, **8**(7), 1837–1866.

13 C. Guan, W. Zhao, Y. Hu, Z. Lai, X. Li, S. Sun, H. Zhang, A. K. Cheetham and J. Wang, Cobalt Oxide and N-Doped Carbon Nanosheets Derived from a Single Two-Dimensional Metal–Organic Framework Precursor and Their Application in Flexible Asymmetric Supercapacitors, *Nanoscale Horiz.*, 2017, **2**(2), 99–105.

14 C. Guan, X. Liu, A. M. Elshahawy, H. Zhang, H. Wu, S. J. Pennycook and J. Wang, Metal–Organic Framework Derived Hollow CoS_2 Nanotube Arrays: An Efficient Bifunctional Electrocatalyst for Overall Water Splitting, *Nanoscale Horiz.*, 2017, **2**(6), 342–348.

15 A. González, E. Goikolea, J. A. Barrena and R. Mysyk, Review on Supercapacitors: Technologies and Materials, *Renewable Sustainable Energy Rev.*, 2016, **58**, 1189–1206.

16 X. Lang, A. Hirata, T. Fujita and M. Chen, Nanoporous Metal/Oxide Hybrid Electrodes for Electrochemical Supercapacitors, *Nat. Nanotechnol.*, 2011, **6**(4), 232–236.

17 H. Pang, Y. Shi, J. Du, Y. Ma, G. Li, J. Chen, J. Zhang, H. Zheng and B. Yuan, Porous Nickel Oxide Microflowers Synthesized by Calcination of Coordination Microflowers and Their Applications as Glutathione Electrochemical Sensor and Supercapacitors, *Electrochim. Acta*, 2012, **85**, 256–262.

18 C. Yuan, X. Zhang, L. Su, B. Gao and L. Shen, Facile Synthesis and Self-Assembly of Hierarchical Porous NiO Nano/Micro Spherical Superstructures for High Performance Supercapacitors, *J. Mater. Chem.*, 2009, **19**(32), 5772–5777.

19 S. Chen, J. Zhu, X. Wu, Q. Han and X. Wang, Graphene Oxide–MnO_2 Nanocomposites for Supercapacitors, *ACS Nano*, 2010, **4**(5), 2822–2830.

20 P. K. Panda, A. Grigoriev, Y. K. Mishra and R. Ahuja, Progress in Supercapacitors: Roles of Two Dimensional Nanotubular Materials, *Nanoscale Adv.*, 2020, **2**(1), 70–108.

21 M. Sricharan, B. Gupta, S. Moolayadukkam and H. S. S. R. Matte, Exfoliation in a Low Boiling Point Solvent and Electrochemical Applications of MoO_3, *Beilstein J. Nanotechnol.*, 2020, **11**, 662–670.

22 Y. Ma, J. He, Z. Kou, A. M. Elshahawy, Y. Hu, C. Guan, X. Li and J. Wang, MOF-Derived Vertically Aligned Mesoporous Co_3O_4 Nanowires for Ultrahigh Capacity Lithium-Ion Batteries Anodes, *Adv. Mater. Interfaces*, 2018, **5**(14), 1800222.

23 Y. Li, Y. Xu, W. Yang, W. Shen, H. Xue and H. Pang, MOF-Derived Metal Oxide Composites for Advanced Electrochemical Energy Storage, *Small*, 2018, **14**(25), 1704435.

 This journal is © The Royal Society of Chemistry 2020

24 H.-L. Jiang, B. Liu, Y.-Q. Lan, K. Kuratani, T. Akita, H. Shioyama, F. Zong and Q. Xu, From Metal–Organic Framework to Nanoporous Carbon: Toward a Very High Surface Area and Hydrogen Uptake, *J. Am. Chem. Soc.*, 2011, **133**(31), 11854–11857.

25 E. Dai, J. Xu, J. Qiu, S. Liu, P. Chen and Y. Liu, Co@Carbon and Co_3O_4@Carbon Nanocomposites Derived from a Single MOF for Supercapacitors, *Sci. Rep.*, 2017, **7**(1), 12588.

26 Y. C. Wang, W. B. Li, L. Zhao and B. Q. Xu, MOF-Derived Binary Mixed Metal/Metal Oxide@carbon Nanoporous Materials and Their Novel Supercapacitive Performances, *Phys. Chem. Chem. Phys.*, 2016, **18**(27), 17941–17948.

27 H. Zhang, X. Liu, Y. Wu, C. Guan, A. K. Cheetham and J. Wang, MOF-Derived Nanohybrids for Electrocatalysis and Energy Storage: Current Status and Perspectives, *Chem. Commun.*, 2018, **54**(42), 5268–5288.

28 M. Toupin, T. Brousse and D. Bélanger, Charge Storage Mechanism of MnO_2 Electrode Used in Aqueous Electrochemical Capacitor, *Chem. Mater.*, 2004, **16**(16), 3184–3190.

29 Y. Hu, Y. Wu and J. Wang, Manganese-Oxide-Based Electrode Materials for Energy Storage Applications: How Close Are We to the Theoretical Capacitance?, *Adv. Mater.*, 2018, 1802569.

30 W. Wei, X. Cui, W. Chen and D. G. Ivey, Manganese Oxide-Based Materials as Electrochemical Supercapacitor Electrodes, *Chem. Soc. Rev.*, 2011, **40**(3), 1697–1721.

31 Y. Wang, W. Lai, N. Wang, Z. Jiang, X. Wang, P. Zou, Z. Lin, H. J. Fan, F. Kang, C.-P. Wong and C. Yang, A Reduced Graphene Oxide/Mixed-Valence Manganese Oxide Composite Electrode for Tailorable and Surface Mountable Supercapacitors with High Capacitance and Super-Long Life, *Energy Environ. Sci.*, 2017, **10**(4), 941–949.

32 R. Das, P. Pachfule, R. Banerjee and P. Poddar, Metal and Metal Oxidenanoparticle Synthesis from Metal Organic Frameworks (MOFs): Finding the Border of Metal and Metal Oxides, *Nanoscale*, 2012, **4**(2), 591–599.

33 M. Huang, F. Li, F. Dong, Y. X. Zhang and L. L. Zhang, MnO_2-Based Nanostructures for High-Performance Supercapacitors, *J. Mater. Chem. A*, 2015, **3**(43), 21380–21423.

34 Y.-Z. Zhang, Y. Wang, Y.-L. Xie, T. Cheng, W.-Y. Lai, H. Pang and W. Huang, Porous Hollow Co_3O_4 with Rhombic Dodecahedral Structures for High-Performance Supercapacitors, *Nanoscale*, 2014, **6**(23), 14354–14359.

35 X. Xu, R. Cao, S. Jeong and J. Cho, Spindle-like Mesoporous α-Fe_2O_3 Anode Material Prepared from MOF Template for High-Rate Lithium Batteries, *Nano Lett.*, 2012, **12**(9), 4988–4991.

36 H. Reinsch and N. Stock, Formation and Characterisation of Mn-MIL-100, *CrystEngComm*, 2013, **15**(3), 544–550.

37 B. Zhang, S. Hao, D. Xiao, J. Wu and Y. Huang, Templated Formation of Porous Mn_2O_3 Octahedra from Mn-MIL-100 for Lithium-Ion Battery Anode Materials, *Mater. Des.*, 2016, **98**, 319–323.

38 R. Das, P. Pachfule, R. Banerjee and P. Poddar, Metal and Metal Oxidenanoparticle Synthesis from Metal Organic Frameworks (MOFs): Finding the Border of Metal and Metal Oxides, *Nanoscale*, 2012, **4**(2), 591–599.

39 X. F. Lu, Y. Chen, S. Wang, S. Gao and X. W. Lou, Interfacing Manganese Oxide and Cobalt in Porous Graphitic Carbon Polyhedrons Boosts Oxygen Electrocatalysis for Zn–Air Batteries, *Adv. Mater.*, 2019, **31**(39), 1902339.

40 U. Holzwarth and N. Gibson, The Scherrer Equation versus the "Debye–Scherrer Equation", *Nat. Nanotechnol.*, 2011, **6**(9), 534.

41 Q. Li, Y. Xu, S. Zheng, X. Guo, H. Xue and H. Pang, Recent Progress in Some Amorphous Materials for Supercapacitors, *Small*, 2018, **14**(28), 1800426.

42 M. Thommes, K. Kaneko, A. V. Neimark, J. P. Olivier, F. Rodriguez-Reinoso, J. Rouquerol and K. S. W. Sing, Physisorption of Gases, with Special Reference to the Evaluation of Surface Area and Pore Size Distribution (IUPAC Technical Report), *Pure Appl. Chem.*, 2015, **87**(9–10), 1051–1069.

43 J. Pike, J. Hanson, L. Zhang and S.-W. Chan, Synthesis and Redox Behavior of Nanocrystalline Hausmannite (Mn_3O_4), *Chem. Mater.*, 2007, **19**(23), 5609–5616.

44 Y. Xiao, Y. Cao, Y. Gong, A. Zhang, J. Zhao, S. Fang, D. Jia and F. Li, Electrolyte and Composition Effects on the Performances of Asymmetric Supercapacitors Constructed with Mn_3O_4 Nanoparticles–Graphene Nanocomposites, *J. Power Sources*, 2014, **246**, 926–933.

45 G. Kéranguéven, J. Faye, S. Royer and S. N. Pronkin, Electrochemical Properties and Capacitance of Hausmannite Mn_3O_4–Carbon Composite Synthesized by *In Situ* Autocombustion Method, *Electrochim. Acta*, 2016, **222**, 755–764.

46 J. Yang and S. Gunasekaran, Electrochemically Reduced Graphene Oxide Sheets for Use in High Performance Supercapacitors, *Carbon*, 2013, **51**, 36–44.

47 M. P. Yeager, W. Du, Q. Wang, N. A. Deskins, M. Sullivan, B. Bishop, D. Su, W. Xu, S. D. Senanayake, R. Si, J. Hanson and X. Teng, Pseudocapacitive Hausmannite Nanoparticles with (101) Facets: Synthesis, Characterization, and Charge-Transfer Mechanism, *ChemSusChem*, 2013, **6**(10), 1983–1992.

48 L. Yang, S. Cheng, X. Ji, Y. Jiang, J. Zhou and M. Liu, Investigations into the Origin of Pseudocapacitive Behavior of Mn_3O_4 Electrodes Using in Operando Raman Spectroscopy, *J. Mater. Chem. A*, 2015, **3**(14), 7338–7344.

49 M. Ghaemi, F. Ataherian, A. Zolfaghari and S. M. Jafari, Charge Storage Mechanism of Sonochemically Prepared MnO_2 as Supercapacitor Electrode: Effects of Physisorbed Water and Proton Conduction, *Electrochim. Acta*, 2008, **53**(14), 4607–4614.

50 H.-L. Guo, X.-F. Wang, Q.-Y. Qian, F.-B. Wang and X.-H. Xia, A Green Approach to the Synthesis of Graphene Nanosheets, *ACS Nano*, 2009, **3**(9), 2653–2659.

51 S. Pei and H.-M. Cheng, The Reduction of Graphene Oxide, *Carbon*, 2012, **50**(9), 3210–3228.

52 B. E. Conway, *Electrochemical Supercapacitors: Scientific Fundamentals and Technological Applications*, Springer Science+Business Media, New York, 1999.

53 Q. Jiangying, G. Feng, Z. Quan, W. Zhiyu, H. Han, L. Beibei, W. Wubo, W. Xuzhen and Q. Jieshan, Highly Atom-Economic Synthesis of Graphene/Mn_3O_4 Hybrid Composites for Electrochemical Supercapacitors, *Nanoscale*, 2013, **5**(7), 2999.

54 T. Xiong, W. S. V. Lee, X. Huang and J. M. Xue, Mn_3O_4/Reduced Graphene Oxide Based Supercapacitor with Ultra-Long Cycling Performance, *J. Mater. Chem. A*, 2017, **5**(25), 12762–12768.

55 Y. Hu, C. Guan, G. Feng, Q. Ke, X. Huang and J. Wang, Flexible Asymmetric Supercapacitor Based on Structure-Optimized Mn_3O_4/Reduced Graphene Oxide Nanohybrid Paper with High Energy and Power Density, *Adv. Funct. Mater.*, 2015, **25**(47), 7291–7299.

56 J.-X. Feng, S.-H. Ye, X.-F. Lu, Y.-X. Tong and G.-R. Li, Asymmetric Paper Supercapacitor Based on Amorphous Porous Mn_3O_4 Negative Electrode and $Ni(OH)_2$ Positive Electrode: A Novel and High-Performance Flexible Electrochemical Energy Storage Device, *ACS Appl. Mater. Interfaces*, 2015, **7**(21), 11444–11451.

57 W. Zilong, Z. Zhu, J. Qiu and S. Yang, High Performance Flexible Solid-State Asymmetric Supercapacitors from MnO_2/ZnO Core–Shell Nanorods//Specially Reduced Graphene Oxide, *J. Mater. Chem. C*, 2014, **2**(7), 1331–1336.

58 H. Xu, X. Hu, H. Yang, Y. Sun, C. Hu and Y. Huang, Flexible Asymmetric Micro-Supercapacitors Based on Bi_2O_3 and MnO_2 Nanoflowers: Larger Areal Mass Promises Higher Energy Density, *Adv. Energy Mater.*, 2015, **5**(6), 1401882.

59 M. F. El-Kady, V. Strong, S. Dubin and R. B. Kaner, Laser Scribing of High-Performance and Flexible Graphene-Based Electrochemical Capacitors, *Science*, 2012, **335**(6074), 1326.

60 X. Lu, M. Yu, G. Wang, T. Zhai, S. Xie, Y. Ling, Y. Tong and Y. Li, H-TiO_2@MnO_2//H-TiO_2@C Core–Shell Nanowires for High Performance and Flexible Asymmetric Supercapacitors, *Adv. Mater.*, 2013, **25**(2), 267–272.

 This journal is © The Royal Society of Chemistry 2020